Role of process type and process conditions on phase content and physical properties of thermal sprayed TiO$_2$ coatings

**J. R. Colmenares-Angulo · V. Cannillo ·
L. Lusvarghi · A. Sola · S. Sampath**

Abstract Thermal spray represents an advantageous technique for depositing large-area titanium dioxide coatings that are of interest for both traditional wear-resistant coatings as well as functional applications such as photo-induced decontamination surfaces. Numerous past studies have examined the phase evolution and properties of TiO$_2$ coatings using different thermal spray processes or parameters. In this paper, an integrated study of thermal sprayed TiO$_2$ was conducted with different thermal spray devices and process parameters for a single feedstock powder comprising the metastable anatase phase. The aforementioned variables are correlated with in-flight particle state (particle temperature and velocity), phase evolution, and coating physical properties. The results are represented through the framework of process maps which connect process parameters with material properties. Based on the phase characterization, an initial exploration of the metastable phase evolution during thermal spray deposition of TiO$_2$ is proposed. Furthermore, the sprayed TiO$_2$ coatings show varying degrees of electrical conductivity associated with process-induced stoichiometric changes (vacancy generation) in the TiO$_2$. The effects of these stoichiometric changes as well as extrinsic microstructural attributes (pores, cracks, interfaces), contribute to the complex electrical response of the coatings. This integrated study provides insights into the process–microstructure–property relationship with the ultimate goal of tailoring the functionality of spray deposited oxide thick films.

Introduction

Titanium dioxide is among the most widely studied metallic oxides from a surface science and engineering point of view [1]. Among its several applications, photo-induced processes are of recent interest including photo-catalysis, photo-induced hydrophilicity, and photovoltaics. These applications present windows of opportunity for environmentally friendly technologies. The aspects that contribute to the applicability of TiO$_2$ for UV photocatalytic applications include its relative low cost, high chemical stability, the creation of highly oxidizing photo-generated holes, and highly reducing photo-generated electrons [2]. Since the first studies on the application of TiO$_2$ for photo-accelerated decomposition of cyanide, research on the subject has expanded to include a wide range of substances such as hydrocarbons [3] and the environmentally harmful nitrogen oxides [4].

Another key characteristic of TiO$_2$ is the relative ease with which oxygen vacancies can be created with changes in processing conditions. The ability to induce such non-stoichiometry will have a direct influence on optical and electrical properties of titanium dioxide, enabling the creation of potentially novel products. Higher level of vacancies will result in a dark and semiconductive (n-type) material while the stoichiometric form will result in a white, highly reflective and electrically insulative ceramic oxide. Given its susceptibility to processing and/or environmental conditions for tailoring electrical properties,

J. R. Colmenares-Angulo (✉) · S. Sampath
Center for Thermal Spray Research Department of Materials Science and Engineering, Stony Brook University, Stony Brook, NY 11794-2275, USA
e-mail: jrcolmena@gmail.com

V. Cannillo · L. Lusvarghi · A. Sola
Dipartimento di Ingegneria dei Materiali e dell'Ambiente, Università di Modena e Reggio Emilia, Via Vignolese 905, 41100 Modena, Italy

TiO$_2$ has been utilized for technological applications such as oxygen pressure sensors [5], electrical varistors [6], and gate insulators [7].

Thermal spray is a widely used processing technique for deposition of metallic and ceramic coatings for a range of applications. In thermal spray, powdered material is heated to a molten or partially molten state and then projected at high velocities onto a surface resulting in a rapidly solidified "splat". A uniform contiguous coating layer is produced by successive impingement of numerous splats. A wide range of ceramic coatings are deposited by thermal spray and TiO$_2$ is among them. TiO$_2$ coatings applied by thermal spray have traditionally been used for applications such as wear protection in shaft-bearing sleeves and are typically applied by atmospheric plasma spray (APS). More recently, other thermal spray variations such as high velocity oxygen fuel (HVOF) or precursor spray have also been utilized.

Recent studies have shown the feasibility of applying thermal spray TiO$_2$ for novel applications such as photo-catalytic [8] and biocompatible [9] coatings and the manufacturing of sputtering targets [10]. Thermal spray coatings have advantages when compared to other methods for photocatalytic applications such as powder dilution in the polluted fluid since the requirement for posterior separation and agglomeration of the powders is avoided [11]. For large area coatings, thermal spray is one the most economical and viable processes, given its high deposition rates and no need for special atmospheric or chemical chambers. Added to its advantages are the durability and high bond strength of the coatings, which give thermal spray a technical advantage for the application in self-decontamination surfaces.

A key issue in thermal spray deposition of TiO$_2$ is the phase formation under non-equilibrium, rapid quenching conditions. The two most common polymorphs of TiO$_2$ are rutile and anatase. Others such as brookite or the reduced magneli phases are rarely observed. There has been an increasing interest to understand mechanisms under which either the stable rutile or the metastable anatase phases are formed in thermally sprayed coatings, since certain phases yield better results for different applications. For example, in a study with the goal of obtaining coatings with enhanced mechanical properties, dense HVOF coatings with rutile as the major phase gave the best results [12]. In a another study, aimed for improving the photocatalytic activity for the decomposition of NO$_x$ suspension, plasma sprayed coatings with over 90% anatase volumetric fraction yielded the most favorable outcome [13].

There is ambiguity concerning the factors that control the phase distributions obtained with thermal sprayed TiO$_2$. Bertrand et al. [14] suggested that anatase is obtained by unmelted fractions of the original feedstock. Nevertheless, this does not explain why some anatase is encountered even when the powder feedstock is purely rutile [15]. However starting from a rutile powder the amount of anatase achieved in the coating is always lower than the amount obtained starting from anatase powder. In addition, other authors believe that increasing the fraction of secondary plasma gas, which usually increases enthalpy and/or thermal conductivity of the plasma, will also increase the amount of the resulting anatase [16]. A theoretical model linking the undercooling levels with the phase distribution of the coatings has been proposed recently [17]. This model suggests that completely molten particles will solidify faster, fostering the nucleation of anatase during solidification. However, this hypothesis appears to contradict the experimental results of previous authors.

The difference of photocatalytical behavior between anatase and rutile is also subject of discussion. For example, it has been suggested that anatase is more efficient in creating electron–hole pairs and absorbing oxygen ions, which will promote a reduction–oxidation reaction [18]. On the other hand, Bacsa [19] affirmed that mixed phases possess a significantly higher catalytic activity due to the improved charge carrier separation in the mixed phase. Other authors have even suggested that the crystallinity of the photocatalytic surface is as important or more important than the phase distribution, since smaller crystallites will promote an abundance of hydroxyl groups, providing a greater number of active sites for the degradation reaction [20].

As explained above, the pathway to phase formation during solidification has not been fully understood for thermal sprayed TiO$_2$. Particle size, morphology, and phase content are known to have an effect on the microstructural features of thermally sprayed coatings [21]. Impurities present in the feedstock powder are known to influence electrical properties of thermally sprayed ceramic oxides [22]. The interaction of the feedstock powder with the hot spray plume is still not completely understood given the short time of the melting process (10^{-5}–10^{-8} s) [23].

When applied by thermal spray, titanium dioxide presents unique characteristics inherently related to the rapid melting and solidification rates of the process, and to the brick-wall structure resulting from the subsequent impingement of molten droplets or splats. The level of oxygen vacancies has been correlated to the in-flight particle temperature of the particles, and subsequently to the resistivity levels of the coatings for the case of air plasma spray [24]. Sharma [25] found that the electrical properties are highly anisotropic due to the differences in stoichiometric distribution among splat regions. Since the interfaces among the splats are mostly parallel to the coating's in-plane direction, the greater in-plane flow of charge (about four orders of magnitude) can be explained

by a higher presence of vacancies at the vicinity of the interfaces. Nevertheless, questions such as the influence of process type and process parameters on the level of electrical anisotropy in thermal spray TiO_2 coatings remain.

These expansive studies have pointed to the complexity in establishing process–structure–property relationships in thermal sprayed TiO_2. Specifically, the effects that selection and sensitivity of process parameters have on phase evolution, microstructure development, and property assessment need to be considered through an integrated strategy. Such an integrated strategy has been demonstrated in the past for thermal spraying of materials such as molybdenum, zirconia, and alumina through the framework of process maps [26, 27]. A process map is an integrated set of relationships that correlate process parameters to coating properties and ultimately to performance indicators. First-order process maps correlate the characteristics of the spray plume, given by combinations of gas flows and energy input parameters such as electric power or combustion heat, with the final molten and kinetic state of the particles in-flight. Second-order process maps will link the particle state to coating physical and functional properties. Detailed description of process maps is reported in the reference [28].

The aim of this study is to contribute to an understanding of phase/microstructure development and its linkage to physical properties of thermally sprayed titanium dioxide coatings conducted within the context of process maps. A notable aspect of this work is the employment of a wide window of particle state variations and the characterization of multiple functional properties by using the versatility and flexibility of various thermal spray process types. Deliberate modification of particle state through the integration of different process conditions and process techniques, including HVOF and APS, is achieved and its subsequent influence on the solidification pathway and trapping of vacancy states will be analyzed. Understanding the influence of such variations will not only shed light on understanding TiO_2 as a material for functional coatings, but also in understanding the complex

non-equilibrium phenomena related to the particle–plume interactions in thermally sprayed particles leading to coatings.

Materials and experimental procedures

All coatings in this study were produced by using a commercially available powder, *Neoxid* 1028 IS40 (Millidyne Oy, Tampere, Finland), an agglomerated and sintered powder with a purity grade of 99.8% with a mean particle size of 16 μm (data reported by the manufacturer). The impurities present mainly consist of less than 30 ppm iron oxide, and less than 0.1 wt.% each of aluminum oxide and silicon oxide. An SEM image of the agglomerated-and-sintered feedstock powder can be observed in Fig. 1. According to X-ray diffraction studies, the phase composition of the feedstock powder was mainly anatase, with the rutile content being less than 4% by volume. The powder was sintered at a temperature close to 900 °C with a short holding time to prevent phase transformations.

Process selection and description (APS, HVOF)

Both APS and HVOF thermal spray processes were investigated. APS and HVOF thermal spray processes operate in different regimes, therefore, significantly differentiating the characteristics of the obtained coatings. In plasma spray, the particles are injected radially into the plasma effluent and the heat transfer occurs external to the nozzle. The plasma consists of a swirl flow mixture of argon (easily ionizable) and hydrogen (highly enthalpic) gases. In addition to melting the particles, this plasma fluid mixture is responsible for the momentum transfer to the particles for projection onto the substrate surface. Different combinations of gas flows, current, and powder injection conditions were examined resulting in significantly different particle conditions in terms of thermal and kinetic energy. Geometrical variables play an important role in defining plasma spray plume–particle interactions; for

Fig. 1 SEM images of the Millydine Neoxid 1028 TiO_2 feedstock powder
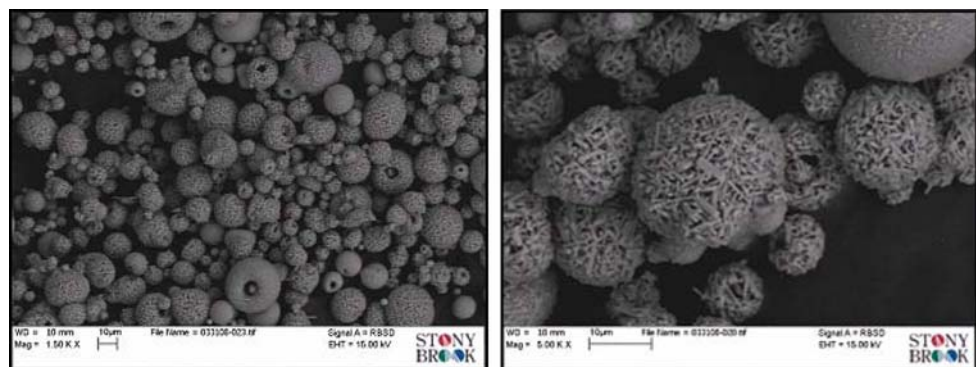
example, the nozzle diameter will have a direct influence on effluent gas velocities, affecting the particle velocity and its residence time in the hottest zones of the plasma [29]. In this study the APS coatings were applied by using nozzle diameters of 5 and 8 mm with a *Plasma Technik F4* commercial plasma spray torch (Sulzer Metco, Westbury, NY). The powder carrier gas flow is known to have a direct effect on the trajectory of the particles when entering the plasma torch, and through active control, the trajectory can be optimized to maximize particle temperature and velocity [30].

In the case of HVOF, the heat input is controlled by the oxygen-to-fuel ratio of the combustion process. The total flow of gases will also have a direct influence on the kinetic energy imparted to the axially injected particles. As a general rule, plasma spray results in hotter but slower particles, being conventionally used for the spraying of high melting temperature materials. HVOF generates much higher particle velocities and in general "cooler" particles, resulting in denser coatings with less oxide content (for case of metals) or chemical heterogeneities caused by extreme heating of particles. The application of HVOF coatings for relatively low melting temperature ceramic oxides (e.g., aluminum oxide) is somewhat recent, but the denser microstructures obtained and the differences in porosity distribution and morphology make HVOF spraying of ceramics a promising technology [27]. In this study two types of commercial HVOF torches were utilized. The first, *Diamond Jet* (Sulzer Metco), uses a mixture of hydrogen fuel, oxygen, and air as flow gases. The second, *HV2000* (Praxair Inc., Indianapolis, IN), uses a mixture of propylene and oxygen as fuel gases, eliminating the heat absorption by the nitrogen in the air, thus resulting in higher particle temperatures. Table 1 describes the different parameters used in this study for the different spraying conditions.

Process diagnostics

Several approaches have been utilized to measure the velocity and/or temperature, and, in some cases, sizes of the in-flight particles within the thermal spray stream. Most commercial sensors will provide basic geometric information of the plasma stream. These sensors have also helped to improve the repeatability of the thermal spray processes. Commercial examples of such sensors are *DPV2000* and *Accuraspray* (both from Tecnar Automation Ltée., St-Bruno, QC, Canada) and *Spray Watch* (Oseir Inc., Finland).

In general, the method for measuring particle velocity consists of measuring the radiation emitted by the particles with two CCD detectors of known geometry. Since the time delay of the signals between the two detectors is

Table 1 Parameters used for processing coatings with different techniques

Condition	Torch hardware	Argon flow (L/min)	Hydrogen flow (L/min)	Current (A)	Powder feed rate (g/min)	Carrier gas (L/min)	Fuel type and flow (L/min)	Oxygen flow (L/min)	Air flow (L/min)	Mean particle temperature (°C)	Mean particle velocity (m/s)
1	APS–F4 8 mm nozzle	47.5	6	550	21	3.9	–	–	–	2713	227
2	APS–F4 8 mm nozzle	35	1	450	21	3.3	–	–	–	2419	147
3	APS–F4 8 mm nozzle	60	2	450	21	4.2	–	–	–	2397	209
4	APS–F4 5 mm nozzle	47.5	6	550	21	6	–	–	–	2691	429
5	APS–F4 5 mm nozzle	35	1	450	21	4.5	–	–	–	2263	301
6	APS–F4 5 mm nozzle	60	2	450	21	7	–	–	–	2368	403
7	HVOF–HV2000	–	–	–	15	10	C_3H_6: 83	240	–	2448	930
8	HVOF–HV2000	–	–	–	15	10	C_3H_6: 42	283	–	2091	737
9	HVOF–diamond jet	–	–	–	15	15	H_2: 563	222	341	1757	762

known, velocity can be determined. In-flight particle temperature is measured by the two wavelength pyrometry method, which consists of quantifying the intensity of the surface radiation emissions at two different wavelengths of the electromagnetic spectrum. This method employs assumptions, such as the particle being a gray body emitter that does not scatter plasma stream emissions. The main difference between *Accuraspray* and *DPV2000* is that the first measures two wavelength pyrometry and the time of flight method of the signals emitted by the complete stream of particles, while the latter has a smaller control volume of measurement, but is able to identify signals emitted from individual particles, resulting in measurements with a higher level of selectivity.

For APS, monitoring the injection of powder into the plasma stream has been proven to be a significant step in controlling and optimizing thermally sprayed coatings [31]. Both *Accuraspray* and *DPV2000* monitor plume geometry by measuring the trajectory that the radially injected particles take after leaving the plasma plume. Another approach to monitor injection is real-time imaging with a laser/camera set-up. Since the plasma emissions are very bright, the camera must be filtered for most visible light wavelengths, and the small fraction of the spectra that the filter will allow the camera to sense is enhanced by the projection of a laser beam into the injection particle stream. This approach is also the fundamental principle of the *Spray Watch/Hi-Watch* commercial thermal spray imaging system, also used here.

In this study, for each selected APS process parameter, the carrier flow was adjusted so that the particles always reached the same plume position (referred to as the sweet spot in reference [32]). This allowed for maximum energy transfer from plasma-to-particle, thus allowing a critical comparison of the process states at the optimum location for each condition. Once the injection was optimized, spray stream diagnostics were conducted using both *Accuraspray* and *DPV2000*. Particle velocity and temperature measurements were obtained through both single particle and ensemble measurements. In all cases the diagnostics measurements were obtained at the nominal spray distance of 100 mm. In the case of HVOF, only *Accuraspray* measurements were utilized and average temperature and velocity of the plume were obtained.

Deposit characterization

Microstructure

Cross sections of the sprayed coatings where characterized by scanning electron microscopy (SEM) (Quanta FEI 200) to observe microstructural features such as porosity and cracks.

Phase content

Phase content of the sprayed coatings were measured by X-ray diffraction (XRD) using a Scintag diffractometer (45 kV and 25 mA; copper Kα source, $\lambda = 1.5405$ Å) in the range of $15°$–$75°$ 2θ with an angular velocity of $0.02°$/s. The phase composition, in terms of anatase and rutile contents, was evaluated using the equation:

$$\text{RVF} = 0.679\frac{I_R}{I_R + I_A} + 0.321\left(\frac{I_R}{I_R + I_A}\right)^2$$

[33] where RVF is the rutile volume fraction, I_A and I_R are the intensities of the anatase (1 0 1) peak ($2\theta = 25.2°$) and rutile (1 1 0) peak ($2\theta = 27.4°$), respectively. XRD was conducted on both the surface of the coatings as well as on powders of the coatings. For the latter, coatings were first separated from the substrate and then crushed into powder in order to promote a random orientation of the crystalline structure given the known existence of preferred crystalline orientations for TiO$_2$ thermally sprayed coatings [34].

Resistivity

As discussed in the introduction, plasma sprayed TiO$_2$ coatings showed semiconducting properties in the as-deposited states associated with process-induced modification of the material stoichiometry. In the earlier work by Sharma et al. only one spray condition was considered and the effect of processing parameters was not investigated [Sharma ref number]. Thus, the electrical properties provide an interesting approach to assess the processing influence on the stoichiometry of the TiO$_2$ particles. Electrical properties of the coatings were evaluated via in-plane electrical resistivity tests (Hewlett Packard 34401A multimeter and Keithley 224 programmable current source). The aluminum substrate was removed by polishing the substrate side to obtain a free-standing form. As far as the electrical resistivity is concerned, a direct current, up to 0.1 A, was applied to the sample and the voltage difference was measured at two points with a known distance between them. The geometry of the sample was quantified with a micrometer. Different measurements of resistance were taken at different probe distances, and, with the known sample dimensions, resistivity was calculated. Through-thickness electrical impedance was also measured for a selected set of process conditions (HP4294A Precision Impedance Analyzer, Hewlett-Packard, CA).

It has been found that through-thickness thermal conductivity of sprayed coatings provides a signature response on the splat–splat interactions and the associated through-thickness transport mechanisms [35]. A Holometrix laser flash instrument for room temperature thermal conductivity

measurement (NETZSCH Instruments, Burlington, MA) was used to measure the through-thickness thermal conductivity in the same selected cases that electrical impedance was measured. The measurement of the thermal diffusivity of the samples was carried out by rapidly heating one side of a sample by a laser and measuring the temperature rise curve on the opposite side as a function of time using an infrared detector. The specific heat is calculated from the data by comparing it to the temperature rise of a reference sample of known specific heat. With the specific heat, thermal diffusivity, and the sample bulk density, the thermal conductivity can be calculated. A detailed explanation of the methodology used can be found in references [36, 37].

Results and discussion

Injection optimization for plasma spray

As previously mentioned, the adjustment of the carrier gas to optimum particle state was managed according to a procedure developed at the Center for Thermal Spray Research at Stony Brook University and described in reference [32]. Previous studies have been primarily conducted on yttria-stabilized zirconia powders. Given that the TiO_2 powder has a significantly lower melting point, it was important to re-establish this result prior to proceeding with parameter variations and process maps. The relationship between the measured particle temperature and plume depth is shown in Fig. 2. These data are obtained for a single plasma spray condition and the results indicate that at a plume depth ≈ 10 mm, a maximum energy transfer was achieved. This plume depth was subsequently fixed for all future runs so that the difference in spraying conditions is not masked by plume location. This procedure has been found to be an important optimization step in establishing process maps.
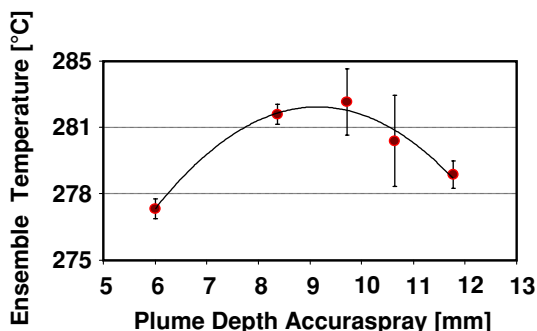
First-order process maps: particle states

As a first step, the effect of varying spray parameters on the properties of thermal spray coatings is best assessed by examining the characteristics of the spray stream generated by the thermal spray torch. To a first approximation, particle temperature (T) and particle velocity (V) are the primary variables affected by the process conditions and flame particle interactions. As such, the first strategy was to map the states of the TiO_2 particles subjected to various spray devices and processing conditions. This is represented in simplified way through a T–V diagram of the spray stream output. Identifying operational zones on the T–V diagram will allow consideration of the results within the context of a process map.

Figure 3 shows the response of the particle state (represented as average temperatures and velocities) as a function of process type, torch, torch geometry, and spray parameters. This expanded first-order process map indicates known responses of process variations, such as the 5 mm nozzle producing higher velocities than the 8 mm nozzle for the case of APS, even though the decreases in temperature were not very significant. It is clear that the higher current conditions (1 and 4) resulted in higher particle temperatures. In the remaining low current conditions, the higher argon total gas flow conditions (6 and 3) yielded higher velocities than for the low gas flow conditions (2 and 5) but not necessarily lower temperatures.

In the case of HVOF spraying, the HV2000 torch resulted in a significantly higher melting of particles, with condition 7 (reducing gas mixture) having higher particle temperature and velocity. The *Diamond Jet* spray, even with the use of a higher enthalpy fuel (H_2) proved unsuitable for the spraying of ceramic materials. It must be mentioned that even though the particle temperature is below the melting point of TiO_2 the reported values constitute averages of a distribution of particle temperatures. As a result, a portion of the *Diamond Jet* sprayed particles

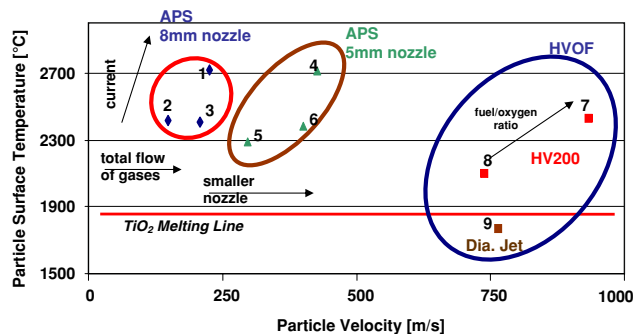Fig. 2 Surface particle temperature as a function of plume geometry

Fig. 3 First-order process map based on mean particle temperature and velocity for the different processes, spray devices, and parameters, and associated characteristics. Error bars were not included for clarity reasons
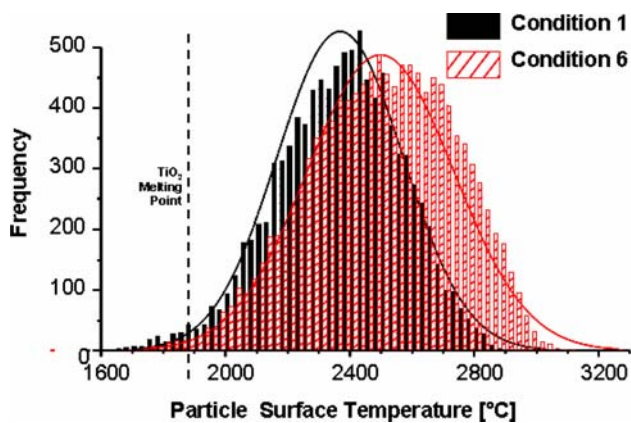
Fig. 4 Particle temperature histogram for two different APS conditions

will be molten or partially molten enabling formation of a coating. Particle temperature histograms for conditions 1 and 6 constructed from individual particle data provided by the *DPV2000* sensor in Fig. 4 are a clear indicator that although the mean values of particle temperature are easily distinguishable in Fig. 3, there is a significant overlapping of individual particle states between the different process conditions.

Second-order process maps: microstructure

Figures 5 and 6 present cross-sectional microstructures of coatings deposited under different conditions. For clarity, the images are relatively overlaid on the first-order process map. Figure 7 presents quantitative values of porosity obtained by image analysis of the SEM micrographs in a

second-order process map. Several important observations can be made:

- For the case of plasma spray, as the velocity increases and temperature decreases, the coating shows an increased porosity content, as shown through the comparison between condition 1 and condition 6. With an increase of both velocity and temperature the opposite effect is found.
- The *HV2000* sprayed coatings where particles attained significantly higher velocities show high density despite somewhat lower particle temperatures. This result is not surprising since the operative mechanisms of deposit formation are different for the plasma and HVOF spray processes (even for ceramics) [27].
- The *Diamond Jet* HVOF sprayed coatings resulted in lower porosity levels than most APS coatings as determined by image analysis. It is clear from the micrographs (Figs. 5 and 6) that the microstructure is highly defective and results in poorly bonded splats. As seen from the first-order map (Fig. 3) the average particle temperature was below the melting point of the TiO_2.

It can be seen from the micrographs that the *HV2000* reducing condition (7) produced dense and uniform coatings given the high momentum at impact. The 8 mm plasma spray condition 1, although presenting the highest particle temperature, has more porosity than for condition 7. The 5 mm nozzle for the APS condition 5 yields the highest porosity of all which can be explained by a combination of low temperature and low particle momentum at impact. *Diamond Jet* sprayed HVOF at condition 9 clearly

Fig. 5 Cross-sectional microstructures of sprayed coatings identified with respect to particle state at 100× magnification
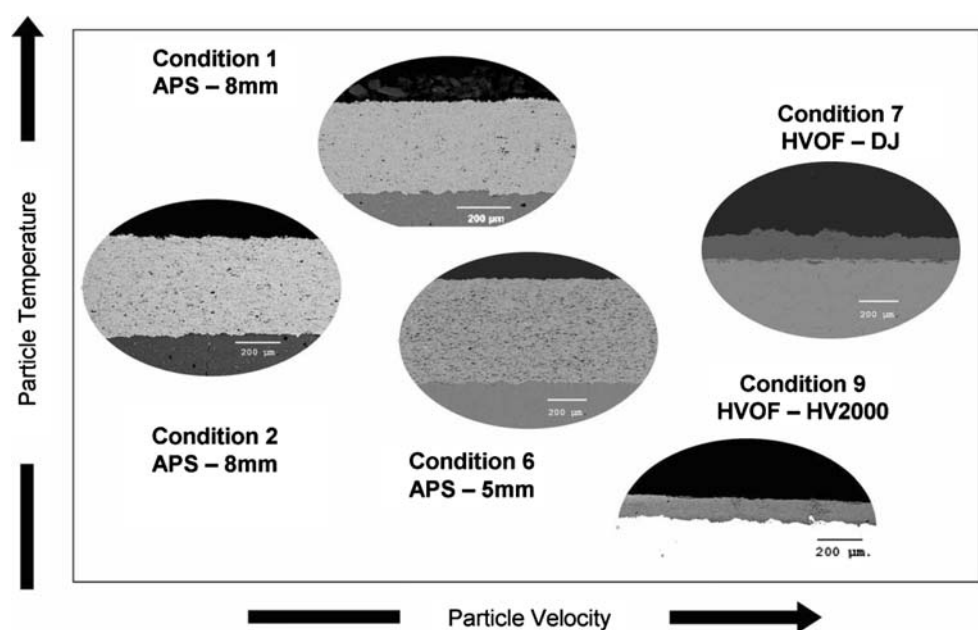
Fig. 6 Cross-section microstructures of sprayed coatings identified with respect to particle state at 1,000× magnification
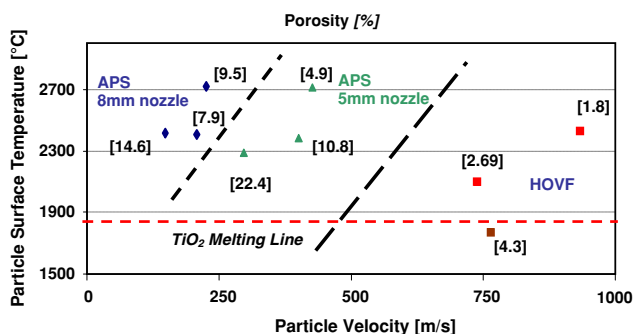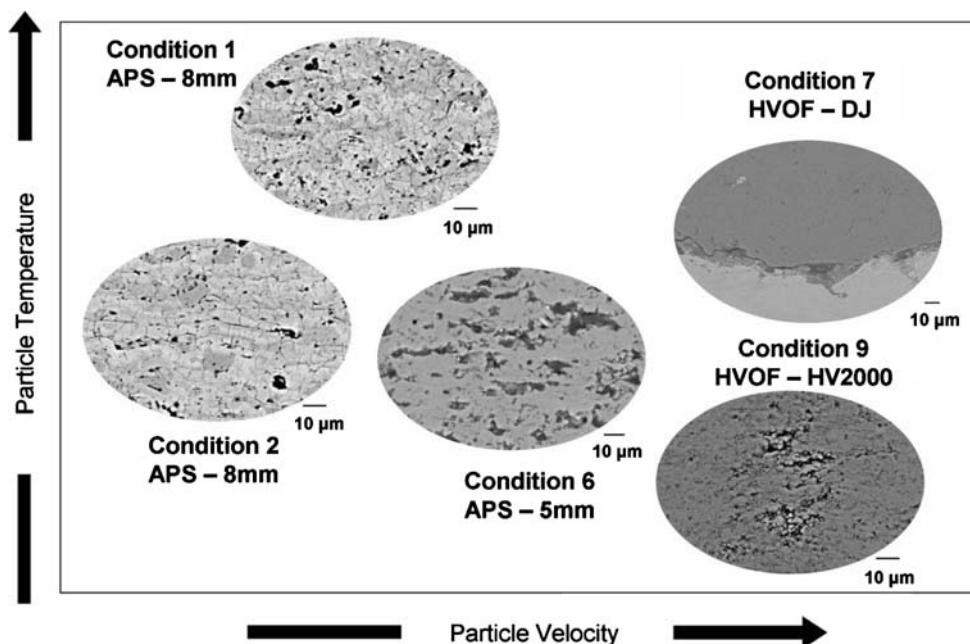

Fig. 7 Porosity of the coatings measured my image analysis of SEM micrographs as a function of particles states represented in a second-order process map

Fig. 8 The relationship between anatase content in the coating and the in-flight particle properties represented as a second-order process map

results in a very defective coating resulting from the high percentage of unmolten or partially molten particles. The differences in porosity levels presented in Fig. 7 are comparable to the observable differences in morphology in Figs. 5 and 6. In the higher magnification micrographs (Fig. 6), clear differences in the quality of intersplat bonding can be observed with the denser coating splats in complete contact and the porous conditions with incomplete bonding.

Second-order process maps: phase composition

Figure 8 shows the second-order process map of the quantitative phase distribution of rutile and anatase in the TiO_2 coatings produced from particles in various T/V states. In general, the results indicate that the coatings contained somewhere between 17 to 40% anatase. Furthermore, it is clear that in general, the anatase content
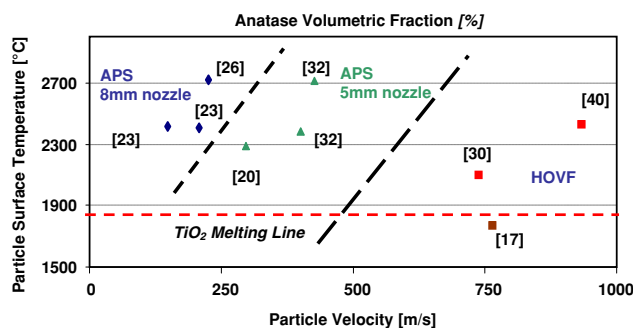
increases as the particle velocity increases suggesting that higher impact velocities can result in generating anatase phase. Increasing particle temperature also appears to result in higher anatase content as is seen for all three operational regimes (8 mm nozzle, 5 mm nozzle, and HVOF). The *Diamond Jet* coating with the lowest temperature and melted particle content resulted in very little anatase in the coating.

It can be observed that for HVOF, a higher anatase fraction was found for condition 7, with the higher particle velocity and the higher particle temperature. The lowest anatase fraction was found in the highly defective *Diamond Jet* sprayed condition 9. This result contradicts the assumption of anatase being the result of unmolten particles. It can also be seen that for the two processes, the condition with the highest particle temperature and velocity results in the most anatase content: condition 1 for APS-8 mm, 4 for APS-5 mm, and 7 for HVOF. This result

agrees with the theory that the higher solidification rates will promote anatase content [17]. This can be explained by the fact that high temperatures will promote the complete melting of the feedstock and particle velocity at impact is expected to influence the thickness of the splats, which also is known to have an effect on the cooling rates of the particles [38]. In fact, particles with higher Reynolds numbers at impact (i.e. higher velocities and temperatures) will spread wider resulting in lower splat thicknesses [39] which in turn will translate into higher splat cooling rates [40]. This is in agreement with a higher content of metastable phase in the high velocity and temperature splats. It is also observed that the conditions with the lowest temperature and velocity combinations for each process resulted in the lowest anatase content (3 for APS-8 mm, 5 for APS-5 mm, and 9 for HVOF).

The phase evolution in the TiO_2 system has been a subject of intense investigation in recent years [1, 2, 8, 13, 14, 34, 41]. The literature in thermal sprayed TiO_2 is much more ambiguous in terms of the observed phases. A number of competing aspects play a role in the preferential emergence of the phases. In our study, the starting feedstock powder was mostly anatase but the resultant coatings were a combination of anatase and rutile. Several scenarios can be considered in this phase evolution:

- Particles that are melted and deposited can exhibit either rutile or anatase depending on the extent of undercooling during solidification. Li and Ishigaki [17] have rationalized that TiO_2 resulting from equilibrium solidification will favor rutile, while anatase nucleation may be favored in enhanced undercooling scenarios. However, it has also been reported that flame or plasma synthesized TiO_2 powders can result in mixtures of anatase and rutile due to partial solidification events and possible recalescence effects.
- During thermal spray TiO_2 splat quenching, the extent of undercooling is perhaps large and as such should favor anatase retention. This is, to a certain extent,

validated in Fig. 8 which indicates that as the impact velocities are increased, the anatase content is increased, resulting from enhanced flattening/solidification rates and thus increased propensity for undercooling.

- A secondary effect perhaps prevalent in thermal sprayed coatings is the entrapment of unmelted or resolidified powders which can produce either rutile or anatase. The possibility of latent heat of solidification emitted by subsequent splat impact in promoting anatase to rutile transformation cannot be discarded, as it has been observed in other ceramic systems for thermal spray that subsequent impact of splats can result in phase transformation [42].

We have proposed herewith a preliminary illustration of a temperature–time transformation diagram that can support the formation of either rutile or anatase formation in the thermal sprayed case. Figure 9 is an illustrative event diagram based on the transformation scenarios proposed by Li and Ishigaki [17]. These results are by no means conclusive but provide a framework for future consideration, especially for thermal spray where the coating phase is highly sensitive to spray parameters and deposition conditions. Ultimately, both the thermodynamic drivers and kinetic aspects have to be considered in these high cooling rate situations. One clear strategy to assess the role of undercooling is to isolate single splats of sprayed droplets and conduct microfocus diffraction experiments. Such studies are underway, with clearly defined particle histories to unequivocally separate effects at least for melt formed rapidly quenched splat situations.

Second-order process maps: in-plane electrical resistivity measurements

The results of the DC electrical resistivity measurements for the TiO_2 coatings are shown in the second-order process map in Fig. 10. As noted in the introduction, thermal

Fig. 9 Visualization of the transformation-time diagrams for TiO_2 solidification during thermal spray. *Note*: All scenarios could be present in the various coatings due to the stochastic nature of the process. Examples presented here indicate the prevalent phase in particles for each condition
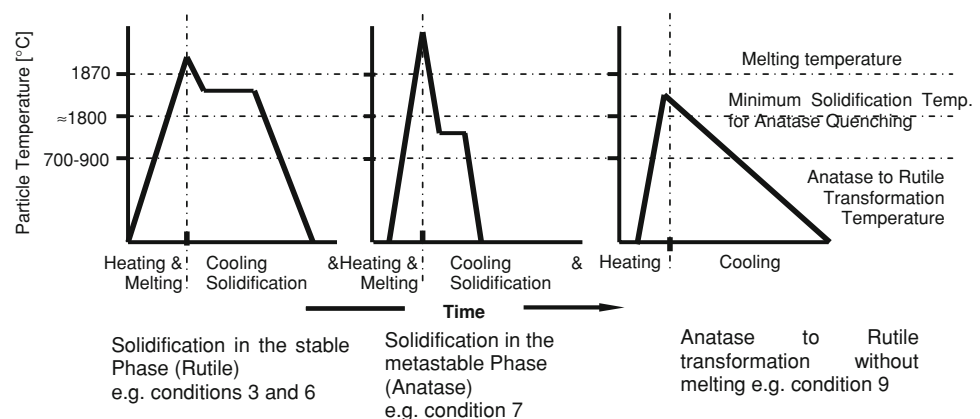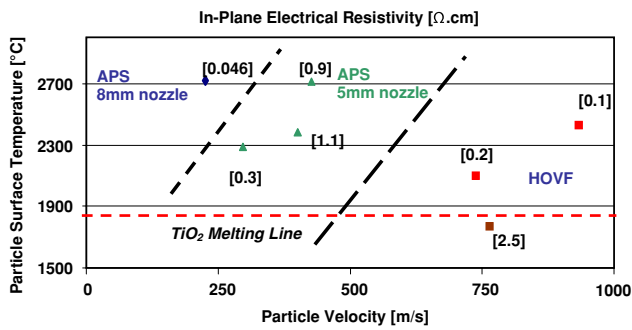
Fig. 10 In-plane electrical resistivity of various thermal sprayed TiO$_2$ coatings represented within the framework of second-order process maps with linkage to particle properties

sprayed TiO$_2$ coatings show room temperature electrical conductivity associated with the presence of vacancies created by the high temperature processing [43].The use of hydrogen as a secondary gas can further accentuate this effect although it is difficult to isolate the role of plasma gas and temperature as these two variables are interrelated. Nevertheless, several important conclusions can be drawn from the second-order process maps in Figs. 7 and 10:

- The coating with highest temperature and lowest velocity (condition 1) results in the lowest resistivity.
- Increasing particle velocity for similar particle temperatures (condition 4) results in an order of magnitude increase in resistivity suggesting that the vacancy concentration is significantly lower. Although differences in coating density exists, it will not account for such a dramatic difference in resistivity.
- The HVOF coatings (conditions 7 and 8) display larger resistivities than for the condition 1 coating despite significantly improved density and interparticle strength.

The complexity of the resistivity results are influenced by both extrinsic properties of the coating, such as the microstructural defects, as well as intrinsic materials properties, such as the vacancy concentration induced by a reduction in the hot plasma. It is clear from these observations that porosity and intersplat bonding are not sufficient indicators to predict coating electrical properties. Electrical transport is also related to the presence of oxygen vacancies created by the process that can act as charge carriers favoring electrical conductivity [44]. The results suggest future pathways for tailoring these two parameters to tune the resistivity of the coatings.

The point defect concentration has a noticeable effect on the optical properties of the coatings [14], since a highly reduced TiO$_2$ surface presents a dark blue tone in contrast to the stoichiometric materials which are white in color [45]. Indeed our starting feedstock powder is white confirming its stoichiometric nature. In our coatings, clear differences in color were also observed among the spray conditions which to a first approximation can be used to differential the intrinsic and extrinsic effects. The coatings with the highest particle temperature (condition 1 APS 8 mm) presented the darkest color while the HVOF coatings were significantly lighter. Condition 1 consisted of both the hottest particles and the most conductive coatings in this study. The higher vacancy concentration for higher particle temperatures can be expected following reference [46].

Among the various APS coatings, the differences are somewhat subtle and difficult to interpret unequivocally. The 5 mm APS sprayed samples (conditions 4, 5, and 6) have a higher velocity and lower residence time in the hot plasma plume, which results in both less vacancies due to decreased reduction and higher porosity levels. This can explain the lower in-plane electrical conductivity compared to the hot APS condition 1. This interpretation can also be extended to the *Diamond Jet* HVOF which results from in the coldest particles but also the ones that are not well melted resulting in a poorly formed microstructure.

Through-thickness thermal conductivity measurements

Thermal conductivity was measured for spraying conditions 1, 6, and 8 of Table 1, with the intention of sampling three very different spraying conditions. As shown in Fig. 11 The HVOF sprayed condition 4, which is also the denser condition (as seen in Figs. 5, 6, and 7) presented the highest through-thickness thermal conductivity (despite not having the highest in-plane electrical conductivity of the 3), while the more porous condition (6-APS 5 mm) presented the lowest thermal conductivity, coinciding with the lowest electrical conductivity. Condition 1 was located at the midpoint of both porosity and thermal conductivity, but of these three selected samples, it is the most electrically conductive sample. These results suggest a higher dependency of the thermal conductivity on extrinsic microstructural features rather than on the intrinsic non-stoichiometry of the
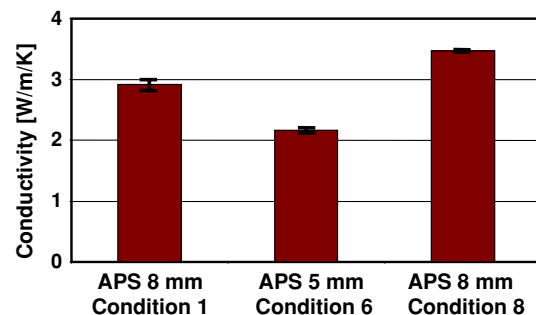

Fig. 11 Through-thickness thermal conductivity of the TiO2 coatings for selected conditions

Table 2 Comparison of the two measures of resistivity for the three different analyzed samples, particle state and through-thickness thermal conductivity are also included for reference

Condition	Resistivity in-plane (Ω cm)	Resistivity through-thickness (Ω cm)	Thermal conductivity (W/m/K)	Porosity (%)	Particle velocity (m/s)	Particle temperature (°C)
1	0.05	7.49×10^4	2.91	9.5	227	2713
6	1.12	1.59×10^5	2.17	22.4	403	2368
8	0.23	3.27×10^3	3.47	2.69	737	2091

material, while the in-plane electrical resistivity is affected by the latter.

AC impedance measurements

The DC resistivity measurements are in-plane measurements with respect to the deposition axis and, as such, measure transport properties along the longer axis of the spray-deposited splats. The AC impedance is a through-thickness measurement and can provide insight into inter-splat bonding. Indeed, the combination of DC resistivity and AC impedance can together provide a full picture of the microstructural and stoichiometry differences among the coatings. At low frequencies—less than 10^4 Hz—the impedance was not dependent on frequency and its value was assumed to represent the coating resistance [43]. Thus, the through-thickness resistivity can be estimated with the known dimensions of the sample and the measured values of resistance.

Table 2 compares the two measures of resistivity for the three different sprayed samples. The through-thickness electrical measurements confirm previous findings of highly anisotropic electrical properties in thermal sprayed TiO_2 coatings. In fact, as proposed by Sharma et al. [44], the boundaries between splats are highly reduced while the core of the splat is more or less stoichiometric. This eases the flow of current through the interfaces, most of which are in-plane within the coating. It can also be observed that the trend for through-thickness resistivity is similar to the through-thickness thermal conductivity; HVOF condition 8 being the most conductive and APS condition 6 the more resistive. This result also indicates higher dependency of the through-thickness transport phenomena in microstructural defects on the coatings rather than vacancy concentration, confirming Sharma's explanation of layered non-stoichiometry effects on in-plane electrical conductivity.

Conclusions

Thermal sprayed TiO_2 coatings are of significant interest for the deposition of large area self-decontamination surfaces utilizing the unique photocatalytic properties of the anatase phase of TiO_2. Considerable research on optimizing TiO_2 phase and properties has been conducted; however, due to differences in processing routes and parametrization, wide-ranging properties are reported.

Properties of TiO_2 coatings processed by thermal spray are dependant on spray method, torch parameters, and torch geometry, all of which ultimately will modify the in-flight characteristics of the particles. This paper seeks an integrated strategy to examine the effects of processing type and process parameters on the phase evolution and microstructure of TiO_2 coatings. The results have been visualized through the framework of first- and second-order process maps which identify the operating domains of the processes.

Metastable anatase phase formation of TiO_2 coatings was found to be promoted by in-flight particle states linked to significant splat flattening and higher solidification rates. The observed results are reconciled through temperature–time transformation type illustrations as a first step toward establishing parametric regimes for understanding phase evolution during thermal spray conditions with the ultimate goal of phase optimization in coatings.

A second contribution through this study is to examine the electrical and thermal transport of the coatings. Thermal sprayed TiO_2 coatings show semiconducting properties through creation of vacancies during the heating/melting stage which are subsequently trapped through rapid solidification. In this study, we have sought to clarify the processing effects on the transport behavior in terms of both the intrinsic defects (vacancies) created through stoichiometric modifications as well as the presence of extrinsic defects such as cracks, pores, and separation. Here again, the results point not only to operative mechanisms but the ability to tune the properties through judicious selection of process type and process parameters. This study sets the stage for both fundamental and practical exploitation of thermal sprayed TiO_2 coatings

References

1. Diebold U (2003) Surf Sci Rep 48:53
2. Fujishima A, Rao TN, Tryk DA (2000) J Photochem Photobiol C Photochem Rev 1:1
3. Hashimoto K, Kawai T, Sakata T (1984) J Phys Chem 88(18):4083
4. Anpo M, Aikawa N, Kubokawa Y, Che M, Louis C, Giamello E (1985) J Phys Chem 89:5689
5. Logothetis E (1980) In: Ceramic engineering and science proceedings, p 1
6. Yan MF, Rhodes WW (1982) Appl Phys Lett 40:536
7. Campbell SA, Kim H-S, Gilmer DC, He B (1999) IBM J Res Dev 43
8. Lee C, Choi H, Lee C, Kim H (2003) Surf Coat Technol 173:192
9. Lima R, Marple B, Li H, Khor K (2006) J Therm Spray Technol 15:623
10. Ohsaki H, Tachibana Y, Hayashi A, Mitsui A, Hayashi Y (1999) Thin Solid Films 351:57
11. Ye F, Ohmori A (2002) Surf Coat Technol 160:62
12. Lima R, Marple B (2003) J Therm Spray Technol 12:360
13. Toma F-L, Sokolov D, Bertrand G, Klein D, Coddet C, Meunier C (2006) J Therm Spray Technol 15:576
14. Bertrand G, Berger-Keller N, Meunier C, Coddet C (2006) Surf Coat Technol 200:5013
15. Lima R, Marple B (2003) J Therm Spray Technol 12:240
16. Wang XY, Liu Z, Liao H, Klein D, Coddet C (2005) Thin Solid Films 473:177
17. Li Y, Ishigaki T (2002) J Cryst Growth 242:511
18. Sclafani A, Herrmann JM (1996) J Phys Chem 100:13655
19. Bach FW, Mohwald K, Rothardt T, Prehm J, Engl L, Hartz K, Droler B (2004) Mater Sci Eng A 383:146
20. Sun J, Gao L, Zhang Q (2003) J Am Ceram Soc 86:1677
21. Wang Z, Kulkarni A, Deshpande S, Nakamura T, Herman H (2003) Acta Mater 51:5319
22. Swindeman CJ, Seals RD, Murray WP, Cooper MH, Forbes KR (1995) An investigation of thermally-sprayed aluminum oxide coatings for high-temperature electrostatic chucks (ESCs). In: Semiconductor manufacturing, IEEE/UCS/SEMI international symposium, Institute of Electrical and Electronics Engineers, Austin, TX, USA, 1995
23. Xiong H-B, Zheng L-L, Li L, Vaidya A (2005) Int J Heat Mass Transfer 48:5121
24. Branland N, Meillot E, Fauchais P, Vardelle A, Gitzhofer F, Boulos M (2006) J Therm Spray Technol 15:53
25. Sharma A (2006) Anisotropic electrical properties of thermal spray coatings: the role of splat boundary interfaces. Doctoral Dissertation, Stony Brook University, 163 pp
26. Sampath S, Jiang X, Kulkarni A, Matejicek J, Gilmore DL, Neiser RA (2003) Mater Sci Eng A 348:54
27. Turunen E, Varis T, Hannula SP, Vaidya A, Kulkarni A, Gutleber J, Sampath S, Herman H (2006) Mater Sci Eng A 415:1
28. Vaidya A, Srinivasan V, Streibl T, Friis M, Chi W, Sampath S (2008) Mater Sci Eng A 497(1–2):239
29. Planche MP, Coudert JF, Fauchais P (1998) Plasma Chem Plasma Process 18:263
30. Zhang W, Zheng L, Zhang H, Sampath S (2007) Plasma Chem Plasma Process 27(6):701
31. Srinivasan V, Vaidya A, Streibl T, Friis M, Sampath S (2006) J Therm Spray Technol 15:739
32. Srinivasan V, Friis M, Vaidya A, Streibl T, Sampath S (2007) Plasma Chem Plasma Process 27:609
33. Burlacov I, Jirkovsky J, Muller M, Heimann RB (2006) Surf Coat Technol 201:255
34. Li JF, Ding CX (1998) J Mater Sci Lett 17:1747
35. McPherson R (1984) Thin Solid Films 112:89
36. Cowan RD (1963) J Appl Phys 34:926
37. Degiovanni A, Laurent M (1986) Rev Phys Appl 21:229
38. Vardelle M, Vardelle A, Leger A, Fauchais P, Gobin D (1995) J Therm Spray Technol 4:50
39. Fauchais P (1995) J Therm Spray Technol 4:3
40. Sampath S, Herman H (1996) J Therm Spray Technol 5:445
41. Lee E-A, Lee S-W, Choi C-H, Kim H-S, Hockey B (2003) Mater Sci Forum 439:8
42. Li L, Kharas B, Zhang H, Sampath S (2007) Mater Sci Eng A 456:35
43. Safai S (1979) In: Materials science and engineering, Stony Brook University, Stony Brook, p 250
44. Sharma A, Gouldstone A, Sampath S, Gambino R (2006) J Appl Phys 100:114906
45. Cronemeyer DC (1952) Phys Rev 87:876
46. Chiang Y-M, Birnie D, Kingery WD (1997) Physical ceramics: principles for ceramics science and engineering. Wiley, New York